Atomic-Scale Mechanism on Nucleation and Growth of Mo2C Nanoparticles Revealed by in Situ Transmission Electron Microscopy

Linfeng Fei,† Sheung Mei Ng,† Wei Lu,† Ming Xu,† Longlong Shu,‡ Wei-Bing Zhang,† Zehui Yong,† Tieyu Sun,† Chi Hang Lam,† Chi Wah Leung,† Chee Leung Mak,*,† and Yu Wang*,‡

†Department of Applied Physics, The Hong Kong Polytechnic University, Hong Kong SAR, China

‡School of Materials Science and Engineering, Nanchang University, Nanchang, Jiangxi 330031, China

*E-mail: apaclmak@polyu.edu.hk (C.L.M.).
*E-mail: wangyu@ncu.edu.cn (Y.W.).

ABSTRACT:

With a similar electronic structure as that of platinum, molybdenum carbide (Mo2C) holds significant potential as a high performance catalyst across many chemical reactions. Empirically, the precise control of particle size, shape, and surface nature during synthesis largely determines the catalytic performance of nanoparticles, giving rise to the need of clarifying the underlying growth characteristics in the nucleation and growth of Mo2C. However, the high-temperature annealing involved during the growth of carbides makes it difficult to directly observe and understand the nucleation and growth processes. Here, we report on the use of advanced in situ transmission electron microscopy with atomic resolution to reveal a three-stage mechanism during the growth of Mo2C nanoparticles over a wide temperature range: initial nucleation via a mechanism consistent with spinodal decomposition, subsequent particle coalescence and monomer attachment, and final surface faceting to well-defined particles with minimum surface energy. These microscopic observations made under a heating atmosphere offer new perspectives toward the design of carbide-based catalysts, as well as the tuning of their catalytic performances.

KEYWORDS:

Transmission electron microscopy, molybdenum carbide, nanoparticles, nucleation, crystal growth, in situ heating

In the chemical industry, an ideal catalyst should be highly active, stable, and abundant in nature at low cost. Having these features, transition metal carbides (TMCs) make a promising alternative for noble-metal-containing catalysts (e.g., Pt, Pd) over a wide spectrum of application scenarios.[1-3] Among them, molybdenum carbide (Mo2C), a representative industrial hydrodesulfurization catalyst,[4,5] also with rising interest associated with methane reforming,[6,7] reduction of CO2 to CO,[8,9] and the emerging hydrogen evolution reaction (HER),[10-15] is currently under intense study. In the past few years, a considerable number of works have contributed to engineering this material at nanometer scale (nanoparticles, nanopolyhedrons, etc.), in order to selectively/simultaneously control its size, shape, and surface structure during its growth.[9-17] Notably, each of these material parameters can greatly affect the electronic structure of the nanoparticles and therefore play a crucial role in determining the catalytic performance of Mo2C (for example, different crystallographic facets are preferred for certain catalytic reactions).[16,18]

Under such circumstances, a thorough understanding on the growth mechanism of Mo2C nanocrystals as well as other TMCs would be greatly helpful for the design and development of novel structures for better catalytic performances. However, the synthesis of Mo2C inevitably involves high-temperature thermal treatment, making direct monitoring of the growth process almost elusive. Very recently, Cao et al. demonstrated their successful attempt in examining the formation of Mo2C from the reaction between Mo and carbon nanotubes, by using combinative spectroscopic methods (including in situ X-ray diffraction and ex situ Raman measurements).[19] However, these spectroscopic approaches or other post-mortem tests (so-called “quench-and-look” approach) fail to eliminate the inhomogeneity across different nanoparticles. Another issue of using these approaches is that important reaction dynamics including the short-lived

intermediated structures during the very-initial stage (such as nucleation process) are very likely to be overlooked because of the limitations of time and length scales used.[20-22] Therefore, it would be essential to develop a realspace, time-resolved, atomic-level observation on the growth of Mo2C nanostructures that can vividly reflect the growth trajectory.

In the past decade, the advancement of technology associated with transmission electron microscopy (TEM) has made it possible for direct observations of the growth process of nanostructured materials at high spatial and temporal resolution upon rational experimental design.[23,24] For example, significant achievements associated with degradation of perovskite solar cells,[25] structural evolution of Pd@CeO2 catalyst,[26] and growth of Y2BaCuO5 nanowire[27] have been made by using advanced in situ TEM configurations. Recently, we have also successfully figured out the growth dynamics of carbon nanostructures and MoS2 flakes in such field.[28,29] Taking the stringent synthesis conditions and the operative experimental design into account, here, we conduct a detailed study on Mo2C growth during in situ TEM annealing experiments as an attempt to reveal the complex nucleation and structural transitions during synthesis. With the assistance of state-of-the-art TEM techniques such as bright-field TEM imaging, high-resolution TEM imaging (HRTEM), selected-area electron diffraction (SAED), and electron energy loss spectroscopy (EELS), our results suggest that Mo and C first nucleate into Mo2C clusters via interfacial diffusion at 800 °C then mutually merge into irregular nanoparticles at 1000 °C before undergoing a sophisticated faceting process to form nanocrystalline polyhedrons at 1200°C. This conceptive study adopts simple TEM configurations to observe the dynamic structural changes of metallic carbide catalysts during chemical reaction and material growth as a function of temperature and time to allow further tailoring the physicochemical properties of catalytic nanoparticles, as well as optimizing the

growth parameters of carbide catalysts. This technique, in general, could be applied to document particle growth other than only carbides.

RESULTS AND DISCUSSION

Mo film was magnetron-sputtered (~1.6 nm in thickness, refer to Figure S1 for atomic force microscopy measurement) onto a heating chip (see Figure S2, also see Methods section for the details), on which an amorphous carbon film (~20 nm in thickness) was predeposited.30 As shown in Figure 1A, a heterostructure composed of a molybdenum film on a carbon film was thus constructed for the in situ annealing experiment. The carbon film served as both the support and the carbon source, and the ultrathin thickness of the heterostructure guarantees a high resolution. The in situ annealing experiments were conducted on a TEM (JEOL JEM-2100F). Results of chemical analysis (energy-dispersive X-ray spectroscopy, EDS) across the figures in Figure S3 showed that the Mo layer was homogeneously distributed on the carbon support, creating an optimal electrontransparent window for our observation. As suggested by Cao et al. in their recent report,19 Mo and C start their reaction in vacuum above ~800 °C. Therefore, the complete sequence of annealing was designed as Figure S4 in our experiment in which the temperature was raised from room temperature to 1200 °C in about 200 min.

Initially, both Mo and C show their amorphous natures at room temperature, as evidenced by the featureless SAED pattern (shown in the first frame in Figure 1B). After reaching 800 °C, a sequence of SAED patterns was taken as a function of heating time to survey the reaction between Mo and C at this temperature. As shown in Figure 1B, blurred diffraction rings emerged after annealing the sample for 5 min, and these rings became progressively sharper and brighter with increasing time, a clear sign of improved crystallinity. Notably, the SAED patterns,

when evident, can all be related to a Mo2C structure with the space group of $Fm\bar{3}m$ (225, JCPDS card No. 15-0457, also see Supplementary note 1), although there is also a possibility that nonstoichiometric phases (MoCx) exist in the early stage. The SAED analysis has confirmed that the reaction/crystallization of molybdenum carbide is initialized at 800 °C, in a good consistency with Cao's report.19 Figure 1C compares two core-level EELS spectra of C K-edge, obtained at room temperature and 800 °C for 30 min, respectively (also refer to Figure S5 for their corresponding zero-loss peaks). The EELS spectrum at room temperature (the black line in Figure 1C) consists of a peak at around 284 eV (originating from the excitations from 1s spin level to empty π* orbits of the sp2-bonded atoms) followed by a diffuse hump at around 289 eV (due to transition from the 1s level to empty σ* orbits at both sp2- and sp3-bonded atoms). The finding is highly consistent with that from previous reports on amorphous carbon structures.31 In contrast, the EELS spectrum at 800 °C (the red line in Figure 1C) displays notable changes: first, the sharper EELS peaks (both π* and σ* peaks) reflect an improvement in crystallization; second, both the π* and σ* peaks show an obvious chemical shift toward the higher-energy region, suggesting the alternation of chemical bonding due to the formation of carbide.32-34 Our findings from the EELS analysis further verify the reaction of Mo and C to yield Mo2C at this stage.

To vividly describe the dynamics of nucleation, in situ micrographs concerning this stage were sequentially captured with respect to heating time (Figure 1D). Interestingly, the sample was found to first (after 7 s) nucleate into interpenetrating nanostructures (web-like structures of 1-2 nm in diameters, see second frame in Figure 1D) from the original amorphous heterostructure. The interpenetrating structures then quickly evolved into twisty rod-like nanostructures (at 31 s, 1-3 nm in diameters, see third frame in Figure 1D). Finally, the structures gradually

transformed into isolated, irregular, anhedral nanoclusters with good homogeneity and monodispersity (at 160 and 1020 s, 2-3 and 2-5 nm in diameter, respectively, see fourth and fifth frames in Figure 1D). It should be noted that in the last frame of Figure 1D, Mo2C nanoclusters possess visible diffraction contrast (the bright halos around some dark crystals) to indicate better crystallinity.

Multiple representative areas across the heating chip were observed synchronously, and the results are well consistent with Figure 1D. Based on all these observations, we further draw simple schematic diagrams to attempt to elucidate the underlying mechanism in this stage. Figure 2A,B outlines the bird-view and side-view of the above process, respectively. Once heated to 800 °C, the Mo layer and the C layer begin their diffusional reaction on the solid-solid interface (namely, the Kirkendall effect),35 in which the predominant process should be the dissolution of C atoms into Mo matrix because of the low diffusion coefficient of Mo, a result from its high melting temperature.36 This unidirectional material transportation contributes to the slight microstructural inhomogeneity of the heterostructure and leads to the formation of asobserved interpenetrating nanostructures.21 Upon continuous heating, the interpenetrating structures act as interconnected transporting channels for mobile species. Therefore, in the succeeding nucleation process, Mo2C clusters increase their contact angle on the carbon support (Figure 2B) to increase their surface areas for structural stabilization, corresponding to the morphological transformation from nanowebs to nanoclusters (Figure 2A). This conclusion is also supported by the mass-thickness contrast of bright-field TEM micrographs as shown in Figure 1D (the last four frames) in which the Mo2C structures became increasingly darker to correspond to the increasingly thicker nanoclusters under the same imaging conditions.

We believe that the above observation of distinctive coarsening of Mo2C nanostructures is indicative of a spinodal decomposition process.37 The interfacial reaction of Mo and C induces topographical fluctuations, leading to the formation of voids in the bicontinuous Mo/C heterostructure. These voids then merge, so that the Mo2C forms interpenetrating nanostructures. Eventually, the interpenetrating nanostructures develop into as-observed Mo2C nuclei as nanoclusters due to Rayleigh instability.38 The increase of aforementioned contact angle with heating time can be further understood by the Young's equation:

$$\theta = cos^{-1}\frac{\Upsilon_{ES} - \Upsilon_{SN}}{\Upsilon_{EN}} \quad (1)$$

where θ is the contact angle, and γES, γSN, and γEN denote the interfacial energies at environment/substrate, substrate/nucleus, and environment/nucleus, respectively (Figure 2B).21 Throughout the above nucleation process, γES can be regarded as constant; while γEN is the average surface energy of all nuclei in environment, which only changes slightly and can also be treated as constant during nucleation. However, γSN grows rapidly during nucleation because of the increasing lattice mismatch between the crystalline nucleus and the substrate due to crystallization of Mo2C. Therefore, the contact angle continues to increase along with the heating time ($0° < \theta < 180°$), resulting in the structural transformation as that shown in Figure 1D.

The annealing temperature was then raised to 1000 °C for further growth of Mo2C. At this temperature, particle coalescence behaviors which lead to rapid growth of nanoparticles were widely identified. Figure

3A shows the sequential images depicting the coalescence behavior of four Mo2C nanoparticles. In this example, initially, one particle (III) met another (IV) to form a dimer (1st frame). The dimer then attacked a third particle (II) to form a twisted chain (2^{nd} frame). Subsequently, the short chain experienced gradual relaxation in its structure, from irregular chain to quasi-spherical particle (V, third to sixth frame) when a fourth particle (I) was approaching it. The four particles eventually merged together and developed into one single-crystalline nanoparticle (7^{th} frame). Such coalescence behavior in crystal growth is frequently reported in many other material systems; for example, gold nanoparticles.39-41 One interesting phenomenon during this process is that particle I changed its outline (denoted by the white arrow in sixth frame) to connect with particle V at a very close situation, possibly caused by the van der Waals attractions.42 Another interesting observation is that annealing at this temperature also led to the presence of a certain population of atomic-scale species across the entire sample (see Figure 3A) that has not been identified previously. These species may be absorbed by particles and hence were also responsible for the particle growth. Based on the above, the growth of nanoparticles should be a collaborative result from simultaneous monomer attachment and particle coalescence, another analogy to previously reported CaCO3 nucleation and Pt colloidal growth.43,44

Thereafter, we captured HRTEM micrograph series on the coalescence event as an attempt to fully understand the underlying mechanism. The in situ lattice-resolved images, as shown in Figure 3B, offer a clear insight into a representative attachment scenario between two neighboring particles. Two particles, with their (111) planes misaligned by ~8°, approached and contacted each other (1st frame in Figure 3B). They then rotated themselves in opposite directions until their lattice planes were close to perfect alignment (~1° mismatch in the second frame in Figure 3B) before coalescing into a single particle. Meanwhile, the small mismatch

induced interfacial defects at these particles' boundary (indicated by yellow arrows), which were eliminated later by successive atom diffusion and mass redistribution driven by the decrease in total system energy (3rd frame in Figure 3B). Eventually, a perfect single crystal without any trace of boundary was formed (4^{th} frame in Figure 3B). The foregoing process represents the typical oriented attachment (OA) mechanism. This mechanism is often found in solution-based synthesis process that benefits from the high mobility and flexibility of either molecular clusters or nanoparticles in solution environment.22 We prove herein this mechanism can also exist in solid-state reactions under certain circumstances, i.e., when the nearby nanoparticles can overcome small lattice mismatch. The order of attachment time consumed in our experiment is also comparable with that during a typical OA process in solution environment (10-100s).42 Notably, although most of the nanoparticles became single-crystalline after coalescence at this stage, their morphologies remained twisted and irregular for an extended period of time (refer to the first frame in Figure S6)

For the irregular (spherical) nanoparticles produced from the above nucleation and growth stages, their surfaces must contain high-index crystallographic planes, which results in high surface energies. However, the Wulff construction has predicted the equilibrium shape of nanocrystals, which follows

$$E = \sum_i E_i = \sum_i \alpha_i \ l_i \tag{2}$$

where E is total energy, Ei is the surface energy for a given facet (i), li is the length of a normal vector drawn from the crystal center to the external facet, and αi is a constant.45 The Wulff construction states that the higher-energy facet grows faster than the lower-energy facet. As a

result, the high-energy facet should eventually disappear during particle development, leading to a nanocrystal terminated by low-index facets.

Therefore, upon further heating at 1200 °C, the above-formed irregular nanoparticles experienced evident facet development, leading to well-defined outlines for minimizing their surface free energies (refer to Figure S6, the overview of the shaping process for massive nanoparticles). In this regime, we found that many nanoparticles tended to shape into truncated cuboctahedrons (see Figure 4A, composed of eight {111}, six {100}, and 12 {110} facets) during extended annealing, an observation frequently found in similar nanoparticle systems.[46,47] Figure S7 shows a simple example to demonstrate the typical faceting process. First, distinct {100} and {111} facets were developed almost simultaneously (at ~800 s) from the original spherical nanoparticle (see the first five frames in Figure S7). At the later stage, {100} and {111} facets shrank, while {110} facets became prominent (see the last three frames in Figure S7) and so well-defined nanoparticles appeared after ~1700 s annealing. This growth sequence is well consistent with the general knowledge that surface energy follows the order of $\gamma\{111\} < \gamma\{100\} < \gamma\{110\}$.[48]

As the electronic structure of nanoparticles shows high dependence on the surface atomic arrangement, atomic-scale observation on the evolution of surface faceting should provide direct insights for designing nanoparticles with desirable surface configurations. Therefore, we further proceed our in situ observations regarding the sophisticated faceting process with atom-resolved HRTEM in the [011] viewing direction as snapshots in Figure 4B. As can be seen, initially, the particle possessed irregular outlines after annealing at 1000 °C, and a clear atomic step can be identified on the surface (denoted by the red line in the first frame in Figure 4B). After 92 s, surface faceting commenced in the second frame of Figure 4B in which the {111} and {100}

facets are identifiable. It was also observed that a few atoms were “missing” on certain facets (denoted by red arrows in the second, fourth, and fifth frames), implying the occurrence of atomic dissociation and redistribution at that moment. (We want to mention it here that atoms directly knocked off by electron beam may be also responsible for such situation.49) It was also noted that the higher-energy {110} facet suddenly appeared at 400 s (the third frame in Figure 4B). However, as the rearrangement of atoms proceeded intensively, evidenced by the variation of atomic columns among third and fifth frames, denoted by red arrows and numbers, we believe it should be an unstable intermediated stage during diffusion of atoms. As expected, the {110} facet disappeared in the fourth frame due to the competition between the surface energy of different facets (i.e., a thermodynamic control process).50 After annealing for 943 s, a well-defined nanoparticle enclosed by {110}, {111}, and {001} facets were formed (the sixth frame in Figure 4B) as sketched in Figure 4A.

The description above clearly shows that the main movement during faceting is mass redistribution caused by the enhanced atom diffusion ability at such elevated temperature. We also found that the attachment of atomic species to nanoparticles (see Figure S7, denoted by yellow arrows) on certain facets also occasionally happens during this process. Therefore, the faceting behavior in our experiment is a combined result of mass migration as well as atomic surface reconstruction.

The aforementioned possible “knock-off” effect inspired us to study the electron beam effect on nanoparticle growth, by comparing different areas across the sample (both irradiated and unirradiated areas) during the annealing experiments. We found that the electron beam has limited effect on different growth stages, especially when a relatively weak beam density was chosen throughout the experiment (see Methods section in SI). For example, as shown in Figure

S7, the unirradiated area possesses similar particle morphology and size distribution as the irradiated one. It can then be concluded that the as-observed dynamics are intrinsic and solely driven by the thermal treatment.

Our study has, hence, extracted the complete growth mechanism of Mo2C nanoparticles with respect to temperature and time, which can be divided into three stages. (I) Nucleation. Mo2C nucleates from the interfacial reaction of molybdenum and carbon, showing a spinodal pathway to gradually increase its surface area and to form nanoclusters. This typical heterogeneous nucleation may share potential similarities with common annealing crystallization and solidstate reaction processes. (II) Particle growth. The Mo2C nanoclusters grow via concurrent monomer attachment and nanoparticle attachment. Particularly, the oriented attachment mechanism was proved to exist in this stage, in parallel with conventional particle coalescence behaviors. (III) Facet development. Based on the principle of minimizing free surface energy, the spherical Mo2C nanoparticles undergo complex surface restructuring to develop flat facets with low-index planes exposed. All the above processes show strong dependence on both annealing temperature and time. This implies that these three stages can be manipulated either thermodynamically or kinetically. Such understanding would make controlling the size, shape, and surface structure of nanoparticles during synthesis possible and offer the freedom to design suitable novel functional nanostructures.

One limitation of our study is that our in situ experiment was performed in a vacuum atmosphere (∼10-5 Pa in TEM column), not suitable for the study of catalysts (e.g., Rh-Pd and Pt-Pd), which show strong dependence of crystal growth behaviors on annealing atmosphere.51,52 We would anticipate that TEM accessories for atmosphere-control be developed in the future, and with that,

it would become possible to achieve better understanding of the atomic-scale kinetic and thermodynamic mechanism of crystal growth under different atmospheres.

In summary, we present a comprehensive observation on the atomic-scale growth dynamics of Mo2C nanocrystals by using collective TEM techniques during in situ annealing. We microscopically reveal a three-stage mechanism during nucleation and growth of Mo2C, which includes a series of important physicochemical changes. Our study paves the way for tailoring carbide materials in size, shape, and surface structure during growth. We also show that the fundamental issues associating with chemical reaction, material growth, and nanomaterial engineering can be better understood by in situ TEM observations with rational experimental design.

AUTHOR INFORMATION

Corresponding Author

*E-mail: apaclmak@polyu.edu.hk (C.L.M.).

*E-mail: wangyu@ncu.edu.cn (Y.W.).

Author Contributions

L.F., C.L.M., and Y.W. conceived the idea and designed the experiment. S.M.N. prepared samples and conducted AFM analysis. L.F. and W.L. conducted in situ TEM experiments. M.X. created schematic figures. L.S., T.S., W.Z., Z.Y., C.H.L., and C.W.L. contributed to discussions. L.F. and Y.W. led experimental data conversion and wrote the manuscript, and all authors commented on it. Y.W. and C.L.M. supervised implementation of project.

Acknowledgments

We acknowledge the use of facilities within the University Research Facility in Materials Characterization and Device Fabrication (UMF)−Centre for Electron Microscopy at The Hong Kong Polytechnic University. This work was supported by The Hong Kong Polytechnic University (project Nos: 1-ZVGH, G-YBJ1) and Nanchang University. Financial support from the Hong Kong Research Grants Council (5016/12P) and National Science Foundation of China (project Nos:51428202, 61302045, 11604135) is also acknowledged.

ASSOCIATED CONTENT

The authors declare no competing financial interest.

Supporting Information Available:

The Supporting Information is available free of charge on the ACS Publications website

Experimental methods, supplementary figures, and note.

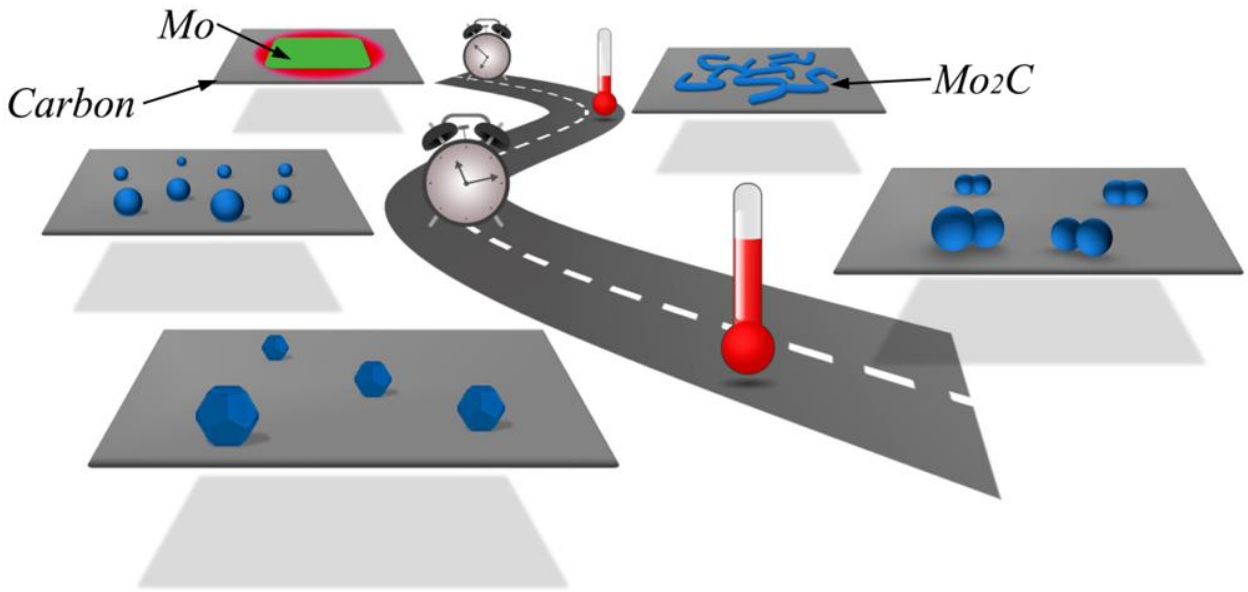

Abstract graphic

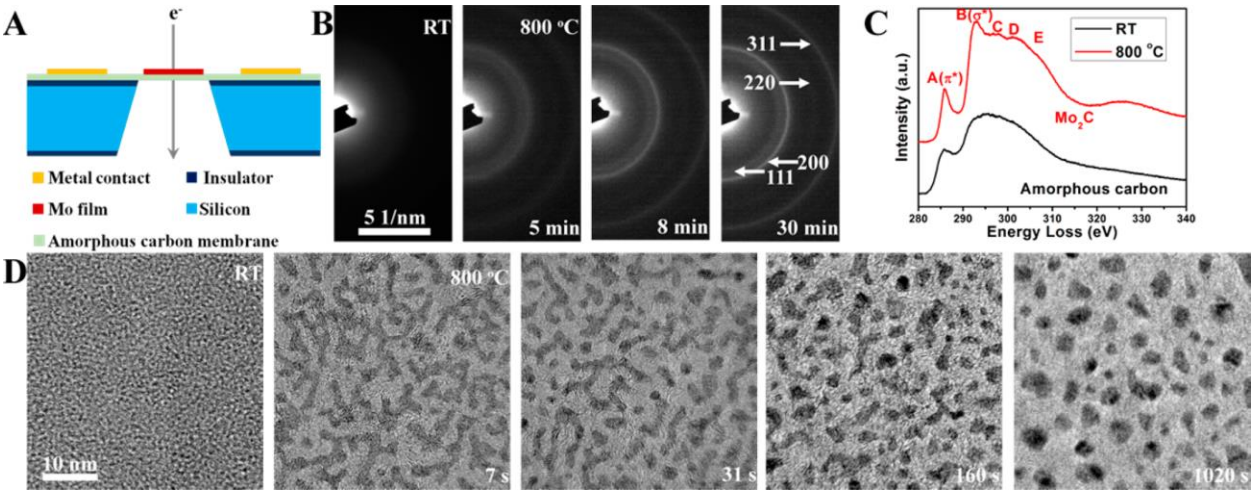

Figure 1. Nucleation dynamics in the formation of Mo2C. (A) Schematic illustration of the experimental setup, showing an amorphous Mo on amorphous C heterostructure was constructed for the in situ observation. (B) The change of SAED patterns as a function of temperature and time. (C) The comparison of core-loss EELS spectrum for C K-edge at room temperature and 800 °C. (D) The representative bright-field TEM images at room temperature and 800 °C, suggesting the sequential transformation from amorphous films to interpenetrated nanowebs, twisted nanorods, and isolated nanoclusters. Time listed in all figures is relative to the reaching of 800 °C. Note that the scale bars in the first frame of (B) and (D) also apply to the subsequent frames.

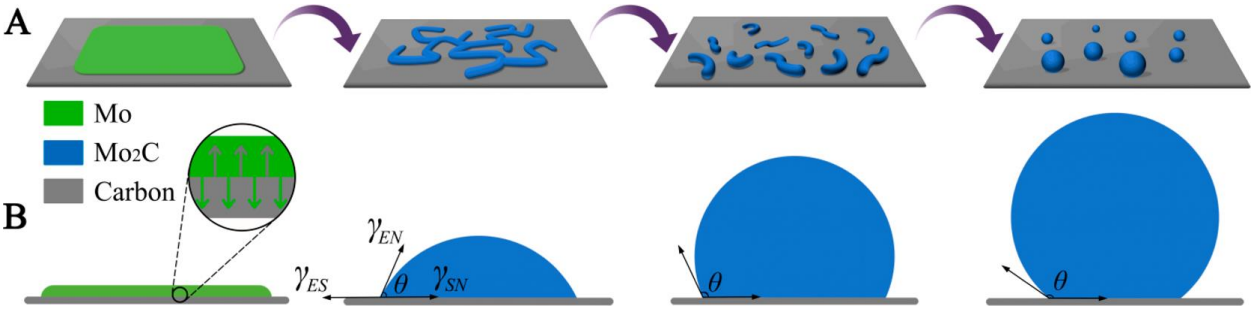

Figure 2. Schematic illustrations for the interfacial nucleation of Mo2C. (A) Bird-view and (B) side-view of the structural transformation process.

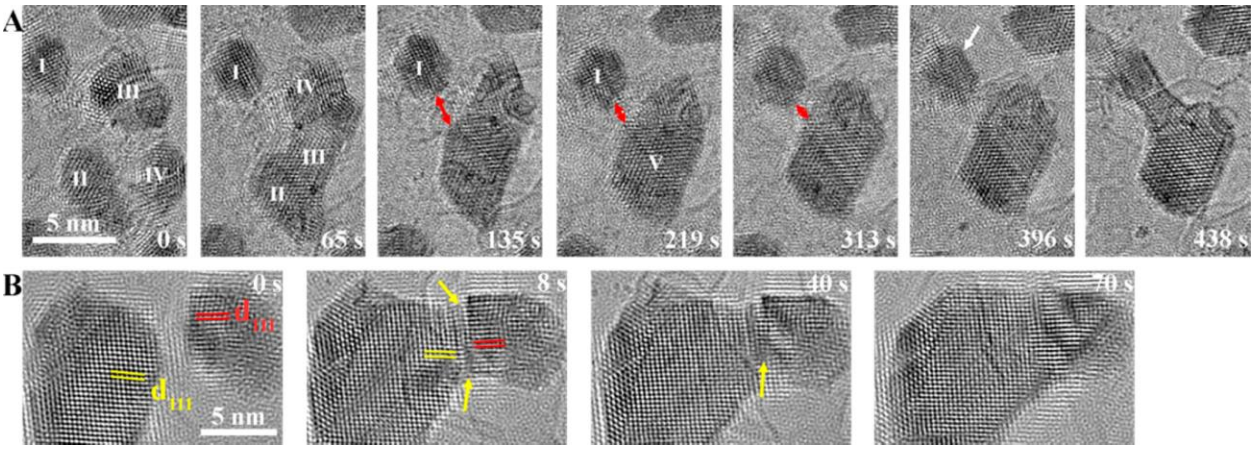

Figure 3. Attachment of irregular Mo2C nanoparticles during annealing at 1000 °C. (A) The series of images shows the coalescence behavior of four particles into one. The Roman numerals denote different nanoparticles. Red arrows denote the distance between particle I and V. (B) Sequential HRTEM images show both crystal orientation change and structural relaxation. Time listed in (A) and (B) is relative to their first frame, respectively. The scale bars in the first frame of (A) and (B) also apply to the subsequent frames.

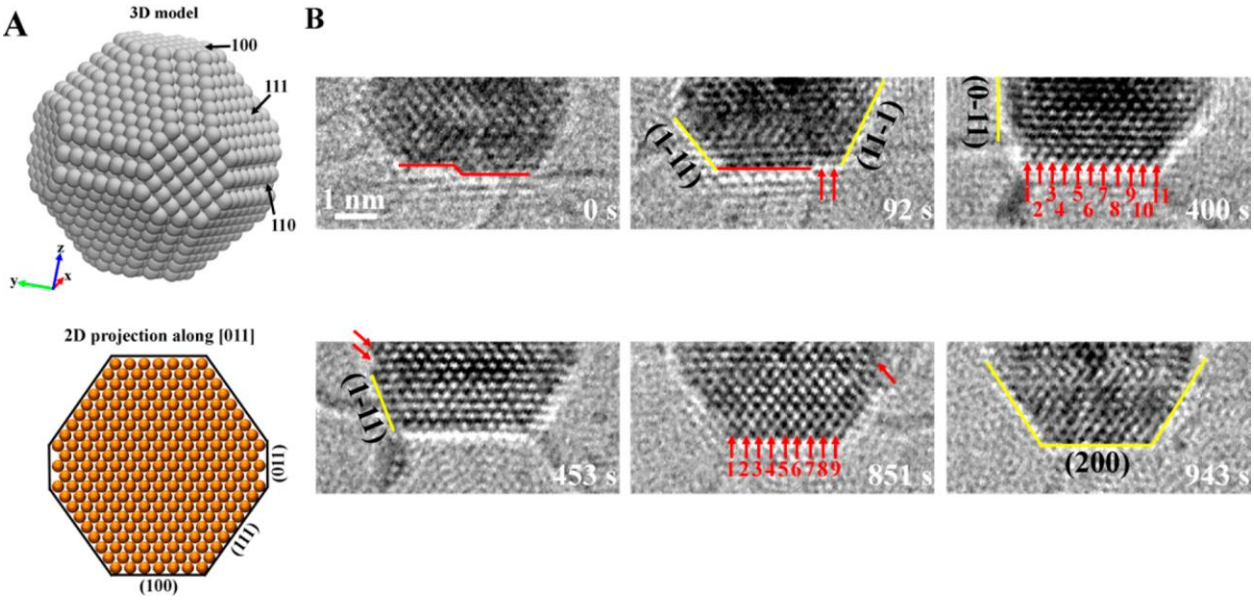

Figure 4. Evolution of nanoparticle facets for Mo2C nanoparticles during annealing at 1200 °C. (A) The 3D model and 2D projection of Mo2C particle as truncated cuboctahedron, enclosed by {100}, {110}, and {111} facets. Only Mo atoms were included to simplify the image. (B) The series of representative micrographs shows the evolution of particle facets. Time listed in all figures is relative to the first frame. The scale bar in the first frame of (B) also applies to the subsequent frames.

REFERENCES

(1) Levy, R. B.; Boudart, M. Platinum-like Behavior of Tungsten Carbide in Surface Catalysis. Science 1973, 181, 547−549.

(2) Chen, J. G. Carbide and Nitride Overlayers on Early Transition Metal Surfaces: Preparation, Characterization, and Reactivities. Chem. Rev. 1996, 96, 1477−1498.

(3) Oyama, S. T. Preparation and Catalytic Properties of Transition Metal Carbides and Nitrides. Catal. Today 1992, 15, 179−200.

(4) Aegerter, P. A.; Quigley, W. W. C.; Simpson, G. J.; Ziegler, D. D.; Logan, J. W.; McCrea, K. R.; Glazier, S.; Bussell, M. E. Thiophene Hydrodesulfurization over Alumina-Supported Molybdenum Carbide and Nitride Catalysts: Adsorption Sites, Catalytic Activities, and Nature of the Active Surface. J. Catal. 1996, 164, 109−121.

(5) Dolce, G. M.; Savage, P. E.; Thompson, L. T. Hydrotreatment Activities of Supported Molybdenum Nitrides and Carbides. Energy Fuels 1997, 11, 668−675.

(6) Claridge, J. B.; York, A. P. E.; Brungs, A. J.; Marquez-Alvarez, C.; Sloan, J.; Tsang, S. C.; Green, M. L. H. New Catalysts for the Conversion of Methane to Synthesis Gas: Molybdenum and Tungsten Carbide. J. Catal. 1998, 180, 85−100.

(7) York, A. P. E.; Claridge, J. B.; Brungs, A. J.; Tsang, S. C.; Green, M. L. H. Molybdenum and Tungsten Carbides as Catalysts for the Conversion of Methane to Synthesis Gas Using Stoichiometric Feedstocks. Chem. Commun. 1997, 1997, 39−40.

(8) Sehested, J.; Jacobsen, C. J. H.; Rokni, S.; Rostrup-Nielsen, J. R.Activity and Stability of Molybdenum Carbide as a Catalyst for CO2 Reforming. J. Catal. 2001, 201, 206−212.

(9) Porosoff, M. D.; Yang, X.; Boscoboinik, J. A.; Chen, J. G. Molybdenum Carbide as Alternative Catalysts to Precious Metals for Highly Selective Reduction of CO2 to CO. Angew. Chem., Int. Ed. 2014, 53, 6705−6709.

(10) Chen, W.-F.; Wang, C.-H.; Sasaki, K.; Marinkovic, N.; Xu, W.; Muckerman, J. T.; Zhu, Y.; Adzic, R. R. Highly Active and Durable Nanostructured Molybdenum Carbide Electrocatalysts for Hydrogen Production. Energy Environ. Sci. 2013, 6, 943.

(11) Li, J.-S.; Wang, Y.; Liu, C.-H.; Li, S.-L.; Wang, Y.-G.; Dong, L.-Z.; Dai, Z.-H.; Li, Y.-F.; Lan, Y.-Q. Coupled Molybdenum Carbide and Reduced Graphene Oxide Electrocatalysts for Efficient Hydrogen Evolution. Nat. Commun. 2016, 7, 11204.

(12) Liao, L.; Wang, S.; Xiao, J.; Bian, X.; Zhang, Y.; Scanlon, M. D.; Hu, X.; Tang, Y.; Liu, B.; Girault, H. H. A Nanoporous Molybdenum Carbide Nanowire as an Electrocatalyst for Hydrogen Evolution Reaction. Energy Environ. Sci. 2014, 7, 387−392.

(13) Wan, C.; Regmi, Y. N.; Leonard, B. M. Multiple Phases of Molybdenum Carbide as Electrocatalysts for the Hydrogen Evolution Reaction. Angew. Chem., Int. Ed. 2014, 53, 6407−6410.

(14) Wu, H. B.; Xia, B. Y.; Yu, L.; Yu, X.-Y.; Lou, X. W. (David). Porous Molybdenum Carbide Nano-Octahedrons Synthesized via Confined Carburization in Metal-Organic Frameworks for Efficient Hydrogen Production. Nat. Commun. 2015, 6, 6512.

(15) Zhao, Y.; Kamiya, K.; Hashimoto, K.; Nakanishi, S. In Situ CO2-Emission Assisted Synthesis of Molybdenum Carbonitride Nanomaterial as Hydrogen Evolution Electrocatalyst. J. Am. Chem. Soc. 2015, 137, 110−113.

(16) Hyeon, T.; Fang, M.; Suslick, K. S. Nanostructured Molybdenum Carbide: Sonochemical Synthesis and Catalytic Properties. J. Am. Chem. Soc. 1996, 118, 5492−5493.

(17) Xu, C.; Wang, L.; Liu, Z.; Chen, L.; Guo, J.; Kang, N.; Ma, X.-L.; Cheng, H.-M.; Ren, W. Large-Area High-Quality 2D Ultrathin Mo2C Superconducting Crystals. Nat. Mater. 2015, 14, 1135−1141.

(18) Wang, T.; Liu, X.; Wang, S.; Huo, C.; Li, Y.-W.; Wang, J.; Jiao, H. Stability of β-Mo2C Facets from Ab Initio Atomistic Thermodynamics. J. Phys. Chem. C 2011, 115, 22360−22368.

(19) Cao, Q.; Han, S.-J.; Tersoff, J.; Franklin, A. D.; Zhu, Y.; Zhang, Z.; Tulevski, G. S.; Tang, J.; Haensch, W. End-Bonded Contacts for Carbon Nanotube Transistors with Low, Size-Independent Resistance. Science 2015, 350, 68−72.

(20) Ross, F. M. Opportunities and Challenges in Liquid Cell Electron Microscopy. Science 2015, 350, aaa9886.

(21) Jiang, Q.; Ward, M. D. Crystallization under Nanoscale Confinement. Chem. Soc. Rev. 2014, 43, 2066−2079.

(22) De Yoreo, J. J.; Gilbert, P. U. P. A.; Sommerdijk, N. A. J. M.; Penn, R. L.; Whitelam, S.; Joester, D.; Zhang, H.; Rimer, J. D.; Navrotsky, A.; Banfield, J. F.; et al. Crystallization by Particle Attachment in Synthetic, Biogenic, and Geologic Environments. Science 2015, 349, aaa6760.

(23) Sinclair, R.; Itoh, T.; Chin, R. In Situ TEM Studies of Metal Carbon Reactions. Microsc. Microanal. 2002, 8, 288−304.

(24) Ramachandramoorthy, R.; Bernal, R.; Espinosa, H. D. Pushing the Envelope of in Situ Transmission Electron Microscopy. ACS Nano 2015, 9, 4675−4685.

(25) Divitini, G.; Cacovich, S.; Matteocci, F.; Cina, L.; Di Carlo, A.; Ducati, C. In Situ Observation of Heat-Induced Degradation of Perovskite Solar Cells. Nat. Energy 2016, 1, 15012.

(26) Zhang, S.; Chen, C.; Cargnello, M.; Fornasiero, P.; Gorte, R. J.; Graham, G. W.; Pan, X. Dynamic Structural Evolution of Supported Palladium−ceria Core−shell Catalysts Revealed by in Situ Electron Microscopy. Nat. Commun. 2015, 6, 7778.

(27) Boston, R.; Schnepp, Z.; Nemoto, Y.; Sakka, Y.; Hall, S. R. In Situ TEM Observation of a Microcrucible Mechanism of Nanowire Growth. Science 2014, 344, 623−626.

(28) Fei, L.; Lei, S.; Zhang, W.-B.; Lu, W.; Lin, Z.; Lam, C. H.; Chai, Y.; Wang, Y. Direct TEM Observations of Growth Mechanisms of Two-Dimensional MoS2 Flakes. Nat. Commun. 2016, 7, 12206.

(29) Fei, L.; Sun, T.; Lu, W.; An, X.; Hu, Z.; Yu, J. C.; Zheng, R.; Li, X.; Chan, H. L. W.; Wang, Y. Direct Observation of Carbon Nanostructure Growth at Liquid−solid Interfaces. Chem. Commun. 2014, 50, 826−828.

(30) Allard, L. F.; Bigelow, W. C.; Bradley, S. A.; Liu, J. A Novel Heating Technology for Ultra-High Resolution Imaging in Electron Microscopes. Microsc. Today 2009, 17, 50.

(31) Mkhoyan, K. A.; Contryman, A. W.; Silcox, J.; Stewart, D. A.; Eda, G.; Mattevi, C.; Miller, S.; Chhowalla, M. Atomic and Electronic Structure of Graphene-Oxide. Nano Lett. 2009, 9, 1058−1063.

(32) Fei, L.; Li, X.; Bi, W.; Zhuo, Z.; Wei, W.; Sun, L.; Lu, W.; Wu, X.; Xie, K.; Wu, C.; et al. Graphene/sulfur Hybrid Nanosheets from a Space-Confined “sauna” Reaction for High-Performance LithiumSulfur Batteries. Adv. Mater. 2015, 27, 5936−5942.

(33) Batson, P. E. Carbon 1s near-Edge-Absorption Fine Structure in Graphite. Phys. Rev. B: Condens. Matter Mater. Phys. 1993, 48, 2608− 2610.

(34) Xu, Z.; Bando, Y.; Liu, L.; Wang, W.; Bai, X.; Golberg, D. Electrical Conductivity, Chemistry, and Bonding Alternations under Graphene Oxide to Graphene Transition as Revealed by in Situ TEM. ACS Nano 2011, 5, 4401−4406.

(35) Paul, A.; van Dal, M. J. H.; Kodentsov, A. A.; van Loo, F. J. J. The Kirkendall Effect in Multiphase Diffusion. Acta Mater. 2004, 52, 623−630.

(36) Zhang, Y. Heterostructures of Single-Walled Carbon Nanotubes and Carbide Nanorods. Science 1999, 285, 1719−1722.

(37) Du, B.; Xie, F.; Wang, Y.; Yang, Z.; Tsui, O. K. C. Dewetting of Polymer Films with Built-in Topographical Defects. Langmuir 2002, 18, 8510−8517.

(38) Rayleigh, L. On the Instability of Jets. Proc. London Math. Soc.1878, 10, 4−13.

(39) Ingham, B.; Lim, T. H.; Dotzler, C. J.; Henning, A.; Toney, M. F.; Tilley, R. D. How Nanoparticles Coalesce: An in Situ Study of Au Nanoparticle Aggregation and Grain Growth. Chem. Mater. 2011, 23, 3312−3317.

(40) Lim, T. H.; McCarthy, D.; Hendy, S. C.; Stevens, K. J.; Brown, S. A.; Tilley, R. D. Real-Time TEM and Kinetic Monte Carlo Studies of the Coalescence of Decahedral Gold Nanoparticles. ACS Nano 2009, 3, 3809−3813.

(41) Wang, J.; Chen, S.; Cui, K.; Li, D.; Chen, D. Approach and Coalescence of Gold Nanoparticles Driven by Surface Thermodynamic Fluctuations and Atomic Interaction Forces. ACS Nano 2016, 10, 2893−2902.

(42) Li, D.; Nielsen, M. H.; Lee, J. R. I.; Frandsen, C.; Banfield, J. F.; De Yoreo, J. J. Direction-Specific Interactions Control Crystal Growth by Oriented Attachment. Science 2012, 336, 1014−1018.

(43) Zheng, H.; Smith, R. K.; Jun, Y.-W.; Kisielowski, C.; Dahmen, U.; Alivisatos, A. P. Observation of Single Colloidal Platinum Nanocrystal Growth Trajectories. Science 2009, 324, 1309−1312.

(44) Nielsen, M. H.; Aloni, S.; De Yoreo, J. J. In Situ TEM Imaging of CaCO3 Nucleation Reveals Coexistence of Direct and Indirect Pathways. Science 2014, 345, 1158−1162.

(45) Ringe, E.; Van Duyne, R. P.; Marks, L. D. Wulff Construction for Alloy Nanoparticles. Nano Lett. 2011, 11, 3399−3403.

(46) Chi, M.; Wang, C.; Lei, Y.; Wang, G.; Li, D.; More, K. L.; Lupini, A.; Allard, L. F.; Markovic, N. M.; Stamenkovic, V. R. Surface Faceting and Elemental Diffusion Behaviour at Atomic Scale for Alloy Nanoparticles during in Situ Annealing. Nat. Commun. 2015, 6, 8925.

(47) Schliehe, C.; Juarez, B. H.; Pelletier, M.; Jander, S.; Greshnykh, D.; Nagel, M.; Meyer, A.; Foerster, S.; Kornowski, A.; Klinke, C.; et al. Ultrathin PbS Sheets by Two-Dimensional Oriented Attachment. Science 2010, 329, 550−553.

(48) Wang, Z. L. Transmission Electron Microscopy of ShapeControlled Nanocrystals and Their Assemblies. J. Phys. Chem. B 2000, 104, 1153−1175.

(49) Kisielowski, C.; Wang, L.-W.; Specht, P.; Calderon, H. A.; Barton, B.; Jiang, B.; Kang, J. H.; Cieslinski, R. Real-Time Sub-Ångstrom Imaging of Reversible and Irreversible Conformations in Rhodium Catalysts and Graphene. Phys. Rev. B: Condens. Matter Mater. Phys. 2013, 88, 24305.

(50) Liao, H.-G.; Zherebetskyy, D.; Xin, H.; Czarnik, C.; Ercius, P.; Elmlund, H.; Pan, M.; Wang, L.-W.; Zheng, H. Facet Development during Platinum Nanocube Growth. Science 2014, 345, 916−919.

(51) Jiang, Y.; Li, H.; Wu, Z.; Ye, W.; Zhang, H.; Wang, Y.; Sun, C.; Zhang, Z. In Situ Observation of Hydrogen-Induced Surface Faceting for Palladium-Copper Nanocrystals at Atmospheric Pressure. Angew. Chem., Int. Ed. 2016, 55, 12427.

(52) Tao, F.; Grass, M. E.; Zhang, Y.; Butcher, D. R.; Renzas, J. R.; Liu, Z.; Chung, J. Y.; Mun, B. S.; Salmeron, M.; Somorjai, G. A. Reaction-Driven Restructuring of Rh-Pd and Pt-Pd Core-Shell Nanoparticles. Science 2008, 322, 932−934.